Journal of Computational Physics 229 (2010) 7594–7608

Contents lists available at ScienceDirect

Journal of Computational Physics

journal homepage: www.elsevier.com/locate/jcp

A pseudo-spectral algorithm and test cases for the numerical solution of the two-dimensional rotating Green–Naghdi shallow water equations

J.D. Pearce [1], J.G. Esler *

Department of Mathematics, University College London, 25 Gower Street, London WC1E 6BT, UK

ARTICLE INFO

Article history:
Received 27 February 2010
Received in revised form 7 June 2010
Accepted 7 June 2010
Available online 1 July 2010

Keywords:
Pseudo-spectral methods
Green–Naghdi equations
Nonlinear waves
Potential vorticity

ABSTRACT

A pseudo-spectral algorithm is presented for the solution of the rotating Green–Naghdi shallow water equations in two spatial dimensions. The equations are first written in vorticity–divergence form, in order to exploit the fact that time-derivatives then appear implicitly in the divergence equation only. A nonlinear equation must then be solved at each time-step in order to determine the divergence tendency. The nonlinear equation is solved by means of a simultaneous iteration in spectral space to determine each Fourier component. The key to the rapid convergence of the iteration is the use of a good initial guess for the divergence tendency, which is obtained from polynomial extrapolation of the solution obtained at previous time-levels. The algorithm is therefore best suited to be used with a standard multi-step time-stepping scheme (e.g. leap-frog).

Two test cases are presented to validate the algorithm for initial value problems on a square periodic domain. The first test is to verify cnoidal wave speeds in one-dimension against analytical results. The second test is to ensure that the Miles–Salmon potential vorticity is advected as a parcel-wise conserved tracer throughout the nonlinear evolution of a perturbed jet subject to shear instability. The algorithm is demonstrated to perform well in each test. The resulting numerical model is expected to be of use in identifying paradigmatic behavior in mesoscale flows in the atmosphere and ocean in which both vortical, nonlinear and dispersive effects are important.

1. Introduction

The Green–Naghdi (GN) shallow water equations [14,28] describe the evolution of a thin layer of fluid under gravity. They differ from the usual shallow water set by an additional term in the momentum equation, to be introduced below, which acts as a short wave dispersion. The dispersive term acts to regularize the shallow water equations, by inhibiting the well-known steepening and breaking of shallow water gravity waves [30]. While not permitting wave-breaking, the GN equations support traveling solitary wave solutions [21], and the GN set in fact reduces to the Korteweg–de Vries equation in the small amplitude limit, under the assumption of uni-directional wave propagation. The exact form of the additional dispersive term that appears in the momentum equations can be found by a standard expansion of the Euler equations in the aspect ratio parameter, and then retaining all terms up to fourth order [14], as opposed to keeping just those terms up to second order as in the derivation of the shallow water equations.

* Corresponding author.
E-mail address: gavin@math.ucl.ac.uk (J.G. Esler).
[1] Supported by the Natural Environment Research Council (Grant No. NER/S/A/2005/13229).

0021-9991/$ - see front matter © 2010 Elsevier Inc. All rights reserved.
doi:10.1016/j.jcp.2010.06.009

Our interest in the GN equations derives from their potential as paradigmatic equations in geophysical fluid dynamics. Miles and Salmon [23] discovered that the GN set can be derived following application of Hamilton's principle to a particular approximation to the Lagrangian of the Euler equations for the evolution of a single layer of fluid with a free surface. The importance of this discovery stems from the fact that the symmetries of the Lagrangian are preserved under Miles and Salmon's approximation, and consequently the GN equations retain conservation properties analogous to those of the full Euler equations [23]. Of particular relevance to geophysical fluid dynamics is that there exists a GN potential vorticity (PV hereafter) that is conserved following fluid particles, meaning that many of the insights due to 'potential vorticity thinking' [19] can be carried across into a system that also supports nonlinear solitary waves. The two-dimensional GN equations, which are easily extended to include the effects of rotation [2,6], may well be the simplest set of hydrodynamic equations that retain a physically meaningful representation of both vorticity dynamics and finite amplitude nonlinear wave behavior. The focus in atmosphere and ocean fluid dynamics is increasingly on mesoscale and sub-mesoscale phenomena where both effects may be important, and for example, the GN set has been used to study flow over topography [26]. The two-layer analog of the GN equations [4] has been used to investigate tidal generation at an ocean ridge and internal solitary wave propagation [16–18]. Further applications of the GN equations include naval hydrodymanics [9–11], the dynamics of the solar tachocline [5] and of bubbly liquids [13].

The above references suggest that fast numerical algorithms to solve the GN equations may be of use in several fields. The challenge in solving the equations stems from the fact that both the leading order time-derivatives and their spatial derivatives appear in nonlinear terms in the equations. Previous authors [7,8,26] have obtained numerical solutions in one-dimension using a finite difference discretization (although note that the algorithm of [26] as presented allows for solution in two-dimensions). In one-dimension the implicit equation for the time-derivatives can be discretized as a tridiagonal matrix equation which must be inverted at each time-step. A similar approach can be used in two-dimensions [9–11], but the matrix necessarily becomes banded, making its inversion and storage expensive as resolution increases. Additionally, naive finite difference methods are known to be relatively diffusive with respect to the parcel-wise conservation of PV described above. Recently,[2] Le Métayer et al. [22] have formulated a finite volume (Godunov-type) algorithm. The scheme invokes a non-local change of variables in order to remove the nonlinear terms involving time-derivatives in favor of a nonlinear elliptic equation for the velocity field which must be solved at each time-step. Several test cases are presented including solitary wave propagation tests similar to those presented below. Detailed comparison between the present scheme and that of Le Métayer et al. awaits a future study.

Our aim here, then, is to develop a new pseudo-spectral algorithm for the two-dimensional GN equations. In the first instance we aim to solve the equations on a doubly-periodic square domain, but the algorithm should be straightforward to generalize to any domain and boundary conditions compatible with pseudo-spectral methods. In Section 2, the GN equations are introduced and re-written in vorticity–divergence form. In Section 3, the pseudo-spectral algorithm is described, and its implementation is discussed. Section 4 describes the first test-case for the resulting numerical model which tests the GN cnoidal wave speeds (in one-dimension). Section 5 describes the second test-case which is a test of parcel-wise PV conservation, which is validated by comparison with a passive tracer, initialized with the same distribution as the PV, and advected by an identical velocity field. Finally, in Section 6 conclusions are presented.

2. The Green–Naghdi equations

2.1. Non-dimensionalization and vorticity–divergence form

The GN equations [14] describe a shallow layer of fluid of local depth $\sigma(\mathbf{x},t)$ moving with a (layer-average) horizontal velocity $\mathbf{u}(\mathbf{x},t)$ under the effect of gravity, over underlying topography. It is assumed here, for simplicity, that the fluid flows over a flat horizontal bottom. Details of how the algorithm can be adapted in the case of non-zero topography are relegated to Appendix A. The rotating GN equations can then be written

$$D\mathbf{u} + f\mathbf{k}\times\mathbf{u} + g\nabla\sigma = -\frac{1}{3\sigma}\nabla\left(\sigma^2 D^2\sigma\right),$$
$$D\sigma + \sigma\nabla\cdot\mathbf{u} = 0,$$

where $\mathbf{k}$ is the vertical unit vector, the fluid is rotating at rate $f/2$, g is the gravitational constant and D is the advective derivative defined by

$$D \equiv \frac{\partial}{\partial t} + \mathbf{u}\cdot\nabla.$$

Non-dimensionalizing these equations, we set

$$\mathbf{u} = U\mathbf{u}^*, \quad t = \frac{L}{U}t^*, \quad \sigma = H\sigma^*, \quad \nabla = \frac{1}{L}\nabla^*, \tag{1}$$

[2] Published after the original submission of this article.

where L is a horizontal length scale, U is a horizontal velocity scale, H is the undisturbed layer depth and time is scaled with L/U. Dropping asterisks, we obtain

$$D\mathbf{u} + \frac{\mathbf{k}\times\mathbf{u}}{\epsilon} + \frac{\nabla\sigma}{F^2} = -\frac{\nu}{3\sigma}\nabla\left(\sigma^2 D^2\sigma\right), \tag{2a}$$

$$D\sigma + \sigma\nabla\cdot\mathbf{u} = 0, \tag{2b}$$

where the square of the aspect ratio ν, the Froude number F, and the Rossby number ϵ, are defined by

$$\nu = \frac{H^2}{L^2}, \quad F = \frac{U}{\sqrt{gH}}, \quad \epsilon = \frac{U}{fL}.$$

Due to the simple form of the Laplacian operator in spectral space and the absence of implicit time dependence in the GN vorticity equation, the GN equations are more amenable to numerical solution in their vorticity–divergence form. The operators $\nabla\cdot$ and $\mathbf{k}\cdot\nabla\times$ are therefore applied to (2a) to obtain

$$\begin{aligned}
\delta_t &= \frac{\zeta}{\epsilon} - \nabla^2\left(\frac{\sigma}{F^2}\right) - \nabla\cdot\left(\frac{\nu}{3\sigma}\nabla(\sigma^2 D^2\sigma) + (\mathbf{u}\cdot\nabla)\mathbf{u}\right),\\
\zeta_t &= -\frac{\delta}{\epsilon} - \nabla\cdot(\mathbf{u}\zeta) - \mathbf{k}\cdot\nabla\times\left(\frac{\nu}{3\sigma}\nabla(\sigma^2 D^2\sigma)\right),\\
\sigma_t &= -\nabla\cdot(\sigma\mathbf{u}),
\end{aligned} \tag{3}$$

where $\delta = \nabla\cdot\mathbf{u}$ is the divergence and $\zeta = \mathbf{k}\cdot\nabla\times\mathbf{u}$ is the vorticity of the flow. Following standard vector calculus manipulations, and using the mass conservation equation ($D\sigma = -\sigma\delta$) to simplify the dispersive terms, (3) becomes

$$\delta_t = \mathbf{k}\cdot\nabla\times\left(\mathbf{u}\left(\zeta+\epsilon^{-1}\right)\right) - \nabla^2\left(\frac{\sigma}{F^2} + \frac{\mathbf{u}\cdot\mathbf{u}}{2} - \frac{\nu\sigma}{3}D(\sigma\delta)\right) + \nabla\cdot\left(\frac{\nu}{3}\nabla\sigma D(\sigma\delta)\right) - \kappa\nabla^4\delta, \tag{4a}$$

$$\zeta_t = -\nabla\cdot\left(\mathbf{u}(\zeta+\epsilon^{-1})\right) + \mathbf{k}\cdot\nabla\times\left(\frac{\nu}{3}\nabla\sigma D(\sigma\delta)\right) - \kappa\nabla^4\zeta, \tag{4b}$$

$$\sigma_t = -\nabla\cdot(\sigma\mathbf{u}) - \kappa\nabla^4\sigma, \tag{4c}$$

where

$$D(\sigma\delta) = \sigma(\delta_t + (\mathbf{u}\cdot\nabla)\delta - \delta^2).$$

In common with previous pseudo-spectral algorithms for the shallow water equations, if turbulent flows are to be simulated, some form of diffusion is necessary to absorb the down-scale cascade in enstrophy. Here, a fourth order hyperdiffusion term $-\kappa\nabla^4$ is added to the tendency of the vorticity, divergence and height fields (see also the further discussion in Section 3.3).

2.2. The Green–Naghdi potential vorticity

It is well-known [23] that there exists a PV, $Q_{GN} = Q_{SW} + Q^*$, associated with the GN Eqs. (2a) and (2b) that is conserved following fluid parcels

$$DQ_{GN} = 0. \tag{5}$$

Here, Q_{SW} is the usual non-dispersive shallow water PV

$$Q_{SW} = \frac{\zeta+\epsilon^{-1}}{\sigma},$$

and Q^* is a 'pseudo potential vorticity' given by

$$Q^* = \frac{\nu}{3\sigma}\mathbf{k}\cdot(\nabla(D\sigma)\times\nabla\sigma). \tag{6}$$

The Green–Naghdi PV will be central to our second numerical test-case described in Section 5.

3. The Green–Naghdi numerical scheme

3.1. The GN equations in spectral space

The appearance of δ_t in (4d) as well as in the right-hand sides of (4a) and (4b) means that at any instant in time (4a) must be treated as a nonlinear PDE in (x,y), to be solved for δ_t. It is therefore convenient to separate the $D(\sigma\delta)$ terms in (4a) and (4b) into two parts-one involving δ_t and one not. It proves convenient to define vector quantities

$$\mathbf{E} = \mathbf{u}(\zeta + \epsilon^{-1}), \quad \mathbf{G} = \frac{v\sigma\nabla\sigma}{3}[(\mathbf{u}\cdot\nabla)\delta - \delta^2], \quad \mathbf{H} = \frac{v\sigma\delta_t\nabla\sigma}{3}, \quad \mathbf{L} = \sigma\mathbf{u},$$

and scalar quantities

$$\mathcal{T} = -\frac{\mathbf{u}\cdot\mathbf{u}}{2} - \frac{\sigma}{F^2} + \frac{v\sigma^2}{3}\left[(\mathbf{u}\cdot\nabla)\delta - \delta^2\right], \quad \mathcal{W} = \frac{v\delta_t}{3}(\sigma^2 - 1).$$

Neglecting the hyperdiffusion terms (see Section 3.3), Eqs. (4a)–(4c) can then be written as

$$\begin{aligned} &\left(1 - \frac{v}{3}\nabla^2\right)\delta_t - \nabla^2\mathcal{W} - \nabla\cdot\mathbf{H} = \mathbf{k}\cdot\nabla\times\mathbf{E} + \nabla^2\mathcal{T} + \nabla\cdot\mathbf{G}, \\ &\zeta_t = -\nabla\cdot\mathbf{E} + \mathbf{k}\cdot\nabla\times(\mathbf{G}+\mathbf{H}), \\ &\sigma_t = -\nabla\cdot\mathbf{L}. \end{aligned} \tag{7}$$

In order to permit the semi-implicit treatment of linear dispersive terms to be described below, a term $-v\nabla^2(\delta_t)/3$ has been grouped with the linear (first) term in the divergence equation of (7). This operation collects terms which are linear in δ_t, relative to a mean reference state at rest with $\sigma = 1$, into a single linear term in (7), and is motivated by the differing treatments of linear and nonlinear terms to be described below. This grouping of the linear dispersive terms proves essential in obtaining fast convergence of the iteration to be described. The remaining terms on the left side of the divergence equation are those nonlinear terms which include the divergence tendency δ_t.

The set (7) can be used as a starting point to adapt the algorithm presented below for any regular two-dimensional domain (e.g. cylindrical, annular, spherical etc.). Here, however, the focus will be on the case of a square $(2\pi \times 2\pi)$ doubly-periodic domain with isotropic resolution (although of course only minor adjustments are required for a rectangular domain of arbitrary length and width and variable resolution in the x and y directions). The prognostic variables σ, δ, ζ are expanded in the usual discrete Fourier transform

$$\sigma(x,y) = \sum_{m=0}^{N/2}\sum_{n=0}^{N-1}\hat{\sigma}_{mn}\exp\{i(mx+ny)\} + \text{c.c., etc.}$$

with the real variables being taken to be defined on a regular $N \times N$ grid. The fast Fourier transform algorithm is used, and is maximally exploited by choosing N to be a power of two (e.g. [3]). Defining

$$\begin{aligned} &\mathcal{M} = -\mathbf{i}\cdot\mathbf{E} + \mathbf{j}\cdot\mathbf{G} \quad \mathcal{N} = \mathbf{i}\cdot\mathbf{G} + \mathbf{j}\cdot\mathbf{E}, \\ &\mathcal{P} = \mathbf{j}\cdot\mathbf{H} \quad \mathcal{Q} = \mathbf{i}\cdot\mathbf{H}, \\ &\mathcal{R} = \mathbf{i}\cdot\mathbf{L} \quad \mathcal{S} = \mathbf{j}\cdot\mathbf{L}, \end{aligned} \tag{8}$$

where $\mathbf{i}$ and $\mathbf{j}$ are the unit vectors in the x and y directions, (7) may be written in terms of spectral coefficients as

$$(\widehat{\delta_t})_{mn} + \frac{im\widehat{\mathcal{Q}}_{mn} + in\widehat{\mathcal{P}}_{mn} + (m^2+n^2)\widehat{\mathcal{W}}_{mn}}{1 + \frac{v}{3}(m^2+n^2)} = -\frac{im\widehat{\mathcal{N}}_{mn} + in\widehat{\mathcal{M}}_{mn} + (m^2+n^2)\widehat{\mathcal{T}}_{mn}}{1 + \frac{v}{3}(m^2+n^2)}, \tag{9}$$

with

$$(\widehat{\zeta_t})_{mn} = -im(\widehat{\mathcal{P}}_{mn} + \widehat{\mathcal{M}}_{mn}) + in(\widehat{\mathcal{N}}_{mn} + \widehat{\mathcal{Q}}_{mn}), \tag{10}$$

$$(\widehat{\sigma_t})_{mn} = im\widehat{\mathcal{R}}_{mn} + in\widehat{\mathcal{S}}_{mn}. \tag{11}$$

The set (9)–(11) is suitable for the time-stepping scheme to be described next.

3.2. Time-stepping and the damped iterative scheme

Time-stepping in the numerical model can be formulated following any explicit multi-step method. Here, a centered-time differencing leap-frog scheme is chosen. Time-stepping takes place in spectral space with the time-step Δt constrained by the Courant–Friedrichs–Lewy (CFL) stability criterion,

$$C_o = \frac{U\Delta t}{\Delta x} < 1. \tag{12}$$

Here, C_o is the Courant number, given in terms of Δt, the grid-spacing Δx and U the maximum flow speed in the domain. In practise, selecting Δt to maintain $C_0 \approx 0.5$, was found to be adequate for stability. The spectral coefficients of the prognostic variables at time level t_{s+1}, where $t_s = t_0 + s\Delta t$, are given by

$$\hat{\delta}^{s+1}_{mn} = \hat{\delta}^{s-1}_{mn} + 2\Delta t(\widehat{\delta}_t)^s_{mn}, \tag{13}$$

with analogous equations for $\hat{\zeta}^{s+1}_{mn}$ and $\hat{\sigma}^{s+1}_{mn}$. Following [15], time-stepping is initiated by a forward Euler time-step of $\Delta t/2$, followed by a centered leap-frog time-step of Δt, and then proceeds with centered time-steps of $2\Delta t$. We note in passing that algorithms using leap-frog time-stepping often require the use of a Robert–Asselin filter [1,27] time filter to control the computational mode. No such filter is required here, most likely because the necessary filtering occurs due to the iteration to be described next.

In order to time-step Eqs. (9)–(11) it is necessary to obtain the divergence tendency at the sth time level $\mathcal{D}^s_{mn} \equiv (\widehat{\delta}_t)^s_{mn}$ from (9). At a given time level (9) can be regarded as a system of nonlinear equations in $\mathcal{D}^s_{mn}$, of the form

$$\mathcal{D}^s_{mn} - \mathcal{F}^s_{mn}(\mathbf{D}^s) = \mathcal{X}^s_{mn}, \tag{14}$$

where $\mathbf{D}^s$ is the matrix with components $\mathcal{D}^s_{mn}$ (with $m \in [0, N/2]$ and $n \in [0, N-1]$), and $\mathcal{F}^s_{mn}$ and $\mathcal{X}^s_{mn}$ correspond to the terms written as fractions on the left and right sides of (9), respectively. Eq. (14) must be solved iteratively at each time-step to obtain $\mathcal{D}^s_{mn}$ before the divergence equation can be updated using (13).

A damped fixed point iterative scheme is used to solve (14) (the $O(N^2)$ dimension of the problem makes naive calculation of the Jacobian for use in Newton-type methods prohibitively expensive). Denoting the dth guess at time level s by the superscript (d,s) the following iteration is used to obtain converged updates for $\mathcal{D}^s_{mn}$, with each iteration being applied to all spectral coefficients (values of m and n) simultaneously,

$$\begin{aligned}
\mathcal{D}^{(0,s)}_{mn} &= \frac{2\left(\hat{\delta}^s_{mn} - \hat{\delta}^{s-1}_{mn}\right)}{\Delta t} - \mathcal{D}^{s-1}_{mn}, \\
\mathcal{D}^{(d+1,s)}_{mn} &= \gamma\left(\mathcal{F}^s_{mn}(\mathbf{D}^{(d,s)}) + \mathcal{X}^s_{mn}\right) + (1-\gamma)\mathcal{D}^{(d,s)}_{mn}, \quad d \geqslant 0.
\end{aligned} \tag{15}$$

The first guess $\mathcal{D}^{(0,s)}_{mn}$ exploits the multi-step method by making a direct linear extrapolation based on the known tendencies at earlier time-levels. The additional accuracy in the first guess due to the extrapolation is found to significantly reduce the number of subsequent iterations necessary for convergence (for certain flows by an order of magnitude or more). The parameter γ controls the relaxation rate of the iteration. This damping constant is left as a free parameter whose optimum value is determined numerically, as discussed in Section 4.3. The iteration is continued until the convergence criterion

$$\frac{\mathrm{Max}_{m,n}\left|\mathcal{D}^{(d,s)}_{mn} - \mathcal{F}_{mn}(\mathbf{D}^{(d,s)}) - \mathcal{X}^s_{mn}\right|}{\mathrm{Max}_{m,n}|\mathcal{D}^{(d,s)}_{mn}|} < \delta_c, \tag{16}$$

is satisfied, with the numerical parameter chosen in the results below to be $\delta_c = 10^{-10}$.

The iteration is applied simultaneously to all wavenumbers rendering it computationally efficient. The spectral coefficients of $\mathcal{M}, \mathcal{N}, \mathcal{R}, \mathcal{S}$ and $\mathcal{T}$ need only be calculated once per time-step at the beginning of the iteration as they do not involve $\mathcal{D}_{mn}$. The spectral coefficients of $\mathcal{P}$, $\mathcal{Q}$ and $\mathcal{W}$, which are required to calculate $\mathcal{F}^s_{mn}(\mathbf{D}^s)$ are re-calculated in real space at each step of the iteration using the new guess for $\mathcal{D}^s_{mn}$, by utilising the fast Fourier transform routine.

3.3. Spectral blocking and the addition of hyperdiffusion terms

The use of spectral methods in the numerical solution of nonlinear partial differential equations can lead to the well-known phenomenon of 'spectral blocking', as discussed in, for example, Boyd [3]. The phenomenon occurs when nonlinear transfer of enstrophy E, defined by $E = \frac{1}{2}\zeta^2$, in spectral space leads to a build-up of enstrophy at high wavenumbers near the truncation limit which cannot then move to sub-grid scales. The result is a gradual, but eventually catastrophic, build-up of numerical noise at the grid-scale. Spectral blocking often occurs in numerical simulation of turbulent geophysical flows, as discussed by Vallis [29].

The problem of spectral blocking is typically handled (e.g. [20]) by the application of a hyperdiffusion operator to damp the highest spectral modes. Following this approach, hyperdiffusion terms parameterizing sub-grid scale mixing are included in the right-hand sides of the evolution Eqs. (4a)–(4c). The hyperdiffusion terms in Eqs. (4a)–(4c) are $-\kappa\nabla^4\delta$, $-\kappa\nabla^4\zeta$ and $-\kappa\nabla^4\sigma$, respectively, where κ is a hyperdiffusion constant. The hyperdiffusion terms are not included in the initial calculation of the tendencies of the prognostic variables, but are added implicitly to the time-stepping so that (13) is modified to become

$$\hat{\delta}^{s+1}_{mn} = \hat{\delta}^{s-1}_{mn} + 2\Delta t\left[(\widehat{\delta}_t)^s_{mn} - \kappa(m^2+n^2)^2\left(\frac{\hat{\delta}^{s+1}_{mn} + \hat{\delta}^{s-1}_{mn}}{2}\right)\right]. \tag{17}$$

Solving for $\hat{\delta}_{mn}^{s+1}$ the updated spectral coefficients for the divergence are then given by

$$\hat{\delta}_{mn}^{s+1} = \frac{(1 - \kappa\Delta t(m^2+n^2)^2)\ \hat{\delta}_{mn}^{s-1} + 2\Delta t(\widehat{\delta_t})_{mn}^{s}}{1 + \kappa\Delta t(m^2+n^2)^2}, \tag{18}$$

with similar expressions for the vorticity and height spectral coefficients, $\hat{\zeta}_{mn}^{s+1}$ and $\hat{\sigma}_{mn}^{s+1}$. The diffusion constant κ scales with $(\Delta x)^2$ where Δx is the grid-spacing, so that

$$\kappa = c^{Diff}(\Delta x)^2,$$

c^{Diff} is a constant independent of resolution. The value of c^{Diff} is set to 8×10^{-3} which was found empirically to be the lowest value at which the hyperdiffusion prevented spectral blocking. The corresponding values of κ for the different resolutions used are shown in Table 1.

3.4. Recovering the horizontal velocities

Once the spectral coefficients $\hat{\delta}_{mn}, \hat{\zeta}_{mn}$ and $\hat{\sigma}_{mn}$ have been obtained at the new timelevel, the horizontal velocities u and v, required for the evaluation of $\mathcal{M}, \mathcal{N}, \mathcal{R}, \mathcal{S}$ and $\mathcal{T}$ during the next time-step, are recovered by a standard technique used in shallow water pseudo-spectral methods. To obtain u and v, the streamfunction ψ and velocity potential χ defined by

$$\nabla^2\psi = \zeta, \quad \nabla^2\chi = \delta,$$

are introduced so that the horizontal velocities may be expressed as

$$u = \chi_x - \psi_y, \quad v = \psi_x + \chi_y.$$

The spectral coefficients $\hat{\psi}_{mn}$ and $\hat{\chi}_{mn}$ may then be obtained by applying the inverse Laplacian operator to $\hat{\zeta}_{mn}$ and $\hat{\delta}_{mn}$ in spectral space (for all spectral coefficients except the $m = 0$, $n = 0$ coefficient) so that the velocity spectral coefficients are given by

$$\hat{u}_{mn} = \frac{im}{(m^2+n^2)}\hat{\delta}_{mn} - \frac{in}{(m^2+n^2)}\hat{\zeta}_{mn}, \quad \hat{v}_{mn} = \frac{im}{(m^2+n^2)}\hat{\zeta}_{mn} + \frac{in}{(m^2+n^2)}\hat{\delta}_{mn}, \tag{19}$$

from which u and v on the grid can be obtained by the inverse Fourier transform.

3.5. The dispersive and diffusive length scales

The addition of hyperdiffusion terms to the evolution Eqs. (4a)–(4c) implies that the solution of the GN equations will be smoothed below a certain length scale. To legitimately claim to be resolving dispersive effects associated with the GN equations, the dispersive length scale must be substantially greater than the diffusive length scale associated with the added hyperdiffusion terms. Linearizing (2a) and (2b) in one horizontal direction and assuming plane wave solutions, the GN linear dispersion relation is given in terms of frequency ω and wavenumber k by

$$\omega = \frac{k}{\sqrt{1 + k^2/3}}.$$

The maximum value of $|\omega''(k)|$ occurs at $k^{Disp} = \frac{\sqrt{3}}{2} \approx 1$, where k^{Disp} can be defined as the characteristic dispersive wavenumber. The requirement that the diffusive length scale is much smaller than the dispersive length scale may therefore be stated as $k^{Diff} \gg 1$, where k^{Diff} is the characteristic diffusive wavenumber. By considering the effect of the hyperdiffusion terms on the tendencies of the prognostic variables in the absence of other terms, k^{Diff} may be defined. In this case, the divergence evolution equation reduces to

$$\delta_t = -\kappa\nabla^4\delta,$$

and similarly for the vorticity and height equations. Considering wave-like solutions to this equation, whose wavenumber is defined to be the characteristic diffusive wavenumber, yields

$$k^{Diff} = \kappa^{-1/4}.$$

Table 1 shows the values of k^{Diff} for the three different resolutions used. Even for the lowest resolution, the condition $k^{Diff} \gg 1$ is satisfied, legitimizing the addition of hyperdiffusion terms to the GN equations to prevent spectral blocking.

Table 1
The table shows the diffusion constant κ and the characteristic dispersive wavenumber k^{Diff} for three different resolutions on a $2\pi \times 2\pi$ domain with $c^{Diff} = 8 \times 10^{-3}$.

Fourier modes	Grid points	Δt	κ	k^{Diff}
64	128	0.03	1.93×10^{-5}	15.1
128	256	0.015	4.82×10^{-6}	21.3
256	512	0.0075	1.21×10^{-6}	30.1

4. Test-case 1: Green–Naghdi cnoidal waves

4.1. Cnoidal wave solutions

The steadily propagating cnoidal wave solutions of the GN equations are well-known [7]. Considering (2a) and (2b) in one horizontal direction and searching for steadily propagating non-rotating ($\epsilon^{-1} = 0$) solutions such that $F = 1$ using the ansatz $u = u(x - ct)$ and $\sigma = \sigma(x - ct)$ where c is the wavespeed, it follows that

$$\begin{aligned} &-cu_x + uu_x + \sigma_x = \frac{\nu}{3\sigma}\frac{\partial}{\partial x}\left(\sigma^2(u-c)\frac{\partial}{\partial x}(u_x\sigma)\right) \\ &u = c\left(1 - \frac{1}{\sigma}\right). \end{aligned} \tag{20}$$

It is assumed in what follows that the undisturbed fluid layer depth is unity. Eliminating u from (20) yields a third order ordinary differential equation which, after some manipulation, may be integrated twice to obtain the cnoidal wave equation

$$\frac{\nu}{6}\sigma_x^2 = -\frac{\sigma^3}{2c^2} + \frac{C_2\sigma^2}{3c^2} - \frac{C_1\sigma}{3c^2} + \frac{1}{2}, \tag{21}$$

where C_1 and C_2 are constants of integration. Eq. (21) has solutions of the form

$$\sigma(x) = a + b\,\mathrm{cn}^2[\alpha x|m], \tag{22}$$

where $\mathrm{cn}[\cdot]$ is a Jacobi elliptic function and where the two relations

$$\begin{aligned} &\alpha^2 = \frac{3b}{4m\nu c^2}, \\ &c^2 = a^3 + a^2 b\left(2 - \frac{1}{m}\right) + ab^2\left(1 - \frac{1}{m}\right), \end{aligned} \tag{23}$$

between the parameters a, b, m and α may be obtained from the substitution of (22) into (21) and the setting of the coefficients of the resulting cubic equation to zero. The requirement that the layer of fluid has an undisturbed depth of unity provides a relation between a and b. We require that the integral of (22) over one wavelength is unity. Since the wavenumber of the GN cnoidal waves is given by

$$k = \frac{\pi\alpha}{K[m]}, \tag{24}$$

this integral may be written as

$$a = 1 - \frac{b\alpha}{2K[m]}\int_{-K[m]/\alpha}^{K[m]/\alpha} \mathrm{cn}^2[\alpha x|m]dx, \tag{25}$$

where $K[m]$ is the complete elliptic integral of the first kind. Using the identity

$$\int \mathrm{cn}^2[\alpha x|m]dx \equiv x - \frac{x}{m} + \frac{1}{\alpha}\left(\frac{E[\mathrm{am}[\alpha x|m]|m]\left(\mathrm{cn}^2[\alpha x|m] + \frac{1}{m} - 1\right)}{\mathrm{dn}[\alpha x|m]\sqrt{1 - m\,\mathrm{sn}^2[\alpha x|m]}}\right),$$

where $E[z|m]$ is the incomplete elliptic integral of the second kind and am, dn and sn are standard Jacobi elliptic functions, the definite integral in (25) may be evaluated to obtain

$$a = 1 - b\left(1 + \frac{E[m] - K[m]}{mK[m]}\right), \tag{26}$$

where $E[m]$ is the complete elliptic integral of the second kind. Notice that α drops out of (25) when the integration takes place and (26) is an expression for a in terms of only b and m. Setting $\nu = 1$, the two parameters b and m may therefore be used to specify the amplitude and steepness, respectively of the cnoidal waves.

4.2. Assessment of GN cnoidal wavespeeds

In Section 4.1, it was demonstrated that the non-rotating GN equations support steadily propagating one-dimensional cnoidal waves. The first test of the numerical model is whether these waves propagate steadily at the velocity c given by (23). Since the domain is assumed to have length 2π and has periodic boundary conditions, we must impose a further constraint that the cnoidal wavelength is 2π. The GN cnoidal wavelength is given by $2K[m]/\alpha$, where $K[m]$ is the complete elliptic integral of the first kind. Therefore, m and b must satisfy the condition

$$K[m] = \alpha(m, b)\pi, \tag{27}$$

where the parameter v is set to unity. We may then choose m to be our one free parameter with b determined by (27). The numerical model is tested with the two cnoidal waves defined by

- STEEP: $m = 0.99$, $c = 0.87800631912$.
- SUPERSTEEP: $m = 0.99999$, $c = 0.81034076434$.

The height field σ and velocity field u of these two waves are shown in Fig. 1. The chosen values of m result in near solitary, cnoidal waves which exhibit large trough-crest asymmetry. The intention here is not to model physically realistic waves but to ensure that the partial differential Eqs. (4a)–(4c) are solved accurately by the numerical model where nonlinearity is strong. The phase speeds at which the two waves propagate are given analytically by (23). The phase speed of a wave in the numerical model may be measured by considering the coefficient of the first Fourier mode of the spectrally transformed σ field. This coefficient is $\hat{\sigma}_{01}$ and is initially at a maximum since the $\sigma(x)$ field is initially chosen to be an even function. The numerically calculated value of c, c_{num}, is obtained from the value of $\hat{\sigma}_{01}$ at some later time, t_n, using

$$c_{num} = \frac{iK[m]}{\alpha\pi t_n} \ln\left(\frac{\hat{\sigma}_{01}^{(t=t_n)}}{\hat{\sigma}_{01}^{(t=0)}}\right), \tag{28}$$

where use has been made of the expression for the GN cnoidal wavenumber (24).

The algorithm was run without hyperdiffusion for one non-dimensional time unit at three different resolutions, corresponding to 64, 128 and 256 Fourier modes in each dimension in the spectral transform. At each resolution c_{num} was obtained using (28) with $t_n = 1$ and the relative error ϵ_c^{mm} calculated using the analytical value of c. The results are shown in Table 2. The values of c_{num} calculated from the numerical model are correct to a high accuracy and converge quadratically towards the analytical value as the resolution is increased. The test was repeated with the wave propagating in the y-direction and the same results were obtained.

4.3. Optimizing the iteration damping coefficient

Several further tests were carried out to examine the robustness of the algorithm. As mentioned previously, the emphasis here is on demonstrating the efficiency of the algorithm at solving the partial differential equations which form the GN set rather than simulating flows of physical relevance. Extreme wave steepening where, in places, $|\nabla\sigma| \geqslant 1$ is therefore considered despite the fact that the GN equations are unlikely to be physically valid for such steep gradients in the free surface.

For a given flow and fixed time-step Δt, there is, in general, a maximum value of the iteration damping constant γ above which the iteration does not converge. Below this maximum is some optimum value γ_{opt} for which the total number of iterations is a minimum. Reducing γ below γ_{opt} increases the number of iterations.

In the absence of an analytical framework to study the dependence of γ_{opt} on the type of flow, the GN cnoidal wave family provides a useful testbed for the examination of the optimum value of γ_{opt}. As shown in Table 2, γ_{opt} must be reduced (i.e. the damping increased) for the SUPERSTEEP wave. Similar behavior has been found for a wide class of flows, i.e. the steeper the free surface the stronger the damping required. To demonstrate this observation quantitatively γ_{opt} was found numerically for six GN cnoidal waves of wavelength 2π. Two of the six waves are the two shown in Fig. 1 and described in Table 2 which were used to test the cnoidal wavespeeds in Section 4.2. Table 3 shows the values of m for all six waves along with the

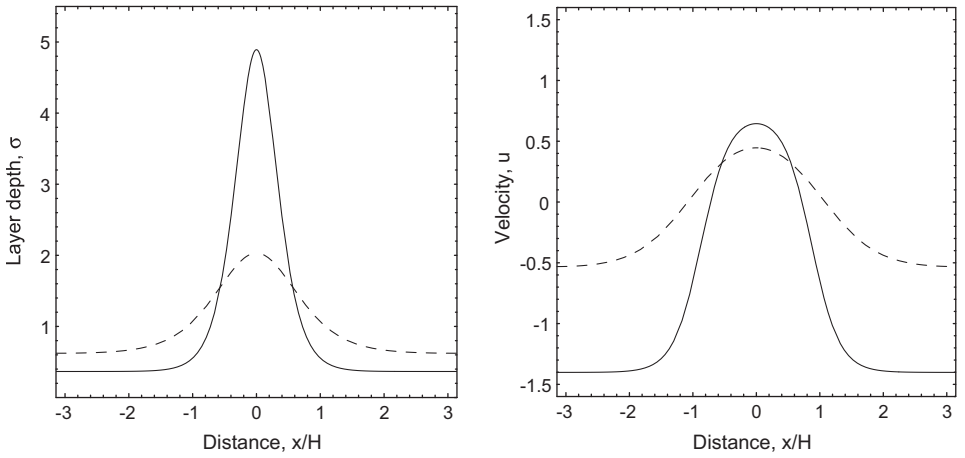

Fig. 1. Layer depth $\sigma(x)$ and velocity $u(x)$ fields for the two GN cnoidal waves with wavelength 2π and $v = 1$. The STEEP wave, with $m = 0.99$, is shown by a dashed line and the SUPERSTEEP wave, with $m = 0.99999$, is shown by a solid line.

Table 2
Table showing the relative error, ϵ_c^{mm}, on the numerically calculated values of c at the three different resolutions corresponding to 256, 128 and 64 Fourier modes in both directions in the spectral transform. The value of c_{num} is obtained using $t_n = 1$ in (28). The initial height and velocity fields for the STEEP [SUPERSTEEP] waves are shown by the dashed [solid] lines in Fig. 1.

Fourier modes	Grid points	Δt	c_{num}	ϵ_c^{mm}	$\epsilon_c^{64}/\epsilon_c^{mm}$
STEEP ($m = 0.99$, $c = 0.87800631912$, $\gamma = 0.4$)					
64	128	0.001	0.87800651056	2.180×10^{-7}	1.0
128	256	0.0005	0.87800636710	5.465×10^{-8}	4.0
256	512	0.00025	0.87800633114	1.369×10^{-8}	15.9
SUPERSTEEP ($m = 0.99999$, $c = 0.81034076434$, $\gamma = 0.07$)					
64	128	0.001	0.81034190086	1.403×10^{-6}	1.0
128	256	0.0005	0.81034105035	3.529×10^{-7}	4.0
256	512	0.00025	0.81034083588	8.827×10^{-8}	15.9

Table 3
The table shows the optimum value of the iteration damping constant γ_{opt} and the average number of iterations n_{iter} for six GN cnoidal waves of wavelength 2π and maximum steepness $|\nabla\sigma|_{max}$. The results were obtained at a resolution of 64×64 Fourier modes for a time-step $\Delta t = 0.001$. No dissipation was added to the GN equations.

m	$\lvert\nabla\sigma\rvert_{max}$	γ_{opt}	n_{iter}
0.9	0.40	0.75	9
0.99	1.28	0.43	27
0.999	2.81	0.23	77
0.9995	3.40	0.19	102
0.99995	5.83	0.10	265
0.99999	7.92	0.08	410

maximum steepness[3] of the waves, $|\nabla\sigma|_{max}$, the optimum value of the iteration damping constant γ_{opt} and the average number of iteration taken n_{iter}. The results were obtained at a resolution of 64×64 Fourier modes for a constant time-step $\Delta t = 0.001$. No dissipation was added to the GN equations by setting $\kappa = 0$. In Fig. 2, the variation of γ_{opt} and n_{iter} with $|\nabla\sigma|_{max}$ is shown. The figure shows the data points corresponding to the six GN cnoidal waves in Table 3. These points are fitted with an exponential function in the case of γ_{opt} and an algebraic function in the case of n_{iter}. Further details about these functions are given in the caption of Fig. 2. Fig. 2 indicates that doubling the maximum steepness of the GN cnoidal wave solution roughly triples the total number of iterations required. The implication for the algorithm is obvious – the numerical model can cope with solutions of the GN equations with a strong gradient in the free surface and velocity fields, but at the price of a substantially longer running time.

The effect on γ_{opt} and n_{iter} of increasing the spatial resolution was also investigated using the cnoidal waves of Table 3. It was found that the value of γ_{opt} did not change appreciably with resolution. However, a fall in n_{iter} of around 20% was observed with a doubling of resolution. For the flows examined in the subsequent chapters, the left-hand panel of Fig. 2 provides a useful indication for what value of γ is appropriate given the maximum steepness of the initial height field. Of course, Fig. 2 can be treated as only a rough guide to more complex or two-dimensional flows. The addition of dissipation to the GN equations will affect γ_{opt} and n_{iter} somewhat.

In the series of nonlinear integrations of two-dimensional flows presented in Section 5 below, the scaling of γ_{opt} with $|\nabla\sigma|_{max}$ shown in Fig. 2 was found to remain a useful guide to the optimal choice of γ. Finally, it should be noted that n_{iter} is a function of the time-step Δt as well as the damping constant γ. The possibility that n_{iter} is reduced at small time-steps Δt has also been considered. The time-step was, however, held constant in the numerical investigations of this section. The maximum value of the time-step is dictated by the CFL criterion (12). It may be reduced, leading to a reduction in n_{iter}, but an increase in the number of time-steps required. It was found, however, that the code performed with optimum efficiency when Δt was close to the value specified by the CFL criterion.

5. Test-case 2: GN potential vorticity conservation

The parcel-wise conservation of Q_{GN} (see Section 2.2) presents a straightforward method of testing the accuracy of the full GN numerical model for complex vortical flows. To ensure that the dispersive terms in the GN equations are tested it is crucial that, during the flow, Q^* is large enough that Q_{GN} differs appreciably from Q_{SW}. It is also preferable to test a flow which develops so that Q_{GN} varies in a complicated way in both horizontal directions. The roll-up of the PV field of a barotropically-

[3] Note that, the relevant measure of wave steepness is the physical non-dimensional slope of the wave, i.e. here $|\nabla\sigma|$ since ν is set equal to unity, but $\nu^{1/2}|\nabla\sigma|$ for cases where a different value of the aspect ratio is taken.

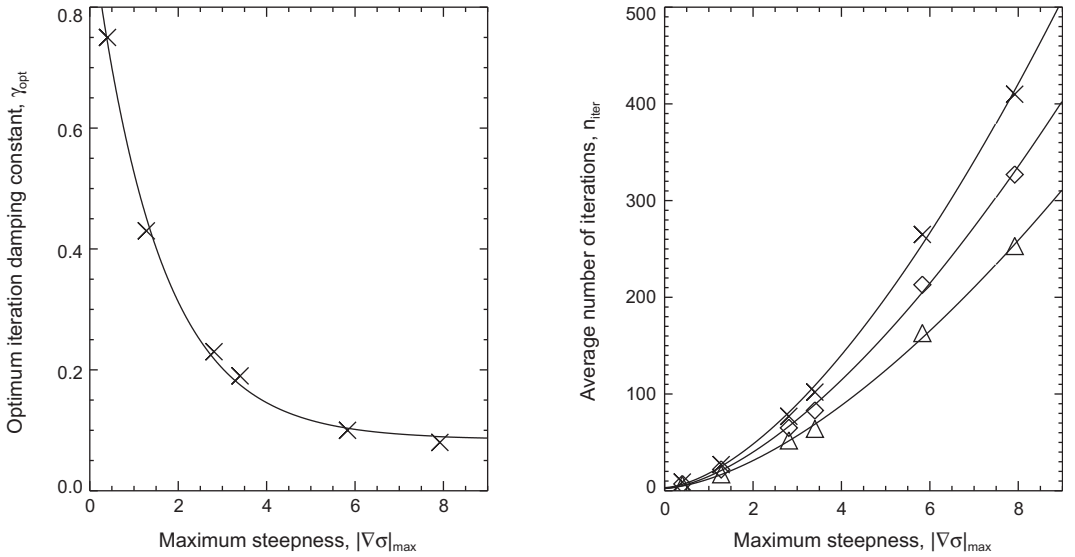

Fig. 2. The figure shows the variation in the optimum value of the iteration damping constant γ_{opt} and the average number of iterations n_{iter} with the maximum steepness of the GN cnoidal waves $|\nabla\sigma|_{max}$. The crosses mark the data points corresponding to the six cnoidal waves in Table 3 for a resolution of 64×64 Fourier modes. The data points are fitted with an exponential function of the form $\gamma_{opt} = a_1 a_2^{|\nabla\sigma|_{max}} + a_3$ on the left-hand plot and a algebraic function of the form $n_{iter} = a_4(|\nabla\sigma|_{max})^{a_5} + a_6$ on the right-hand plot. The constants a_i were found using a gradient-expansion least-squares method and are given by $a_1 = 0.856$, $a_2 = 0.516$, $a_3 = 0.085$, $a_4 = 14.7$, $a_5 = 1.61$ and $a_6 = 3.27$. The results obtained at resolutions corresponding to 128×128 Fourier modes (diamonds) and 256×256 Fourier modes (triangles) are shown in the right-hand panel. In the left-hand panel there was no appreciable change in the positions of the points with resolution No dissipation was added to the GN equations.

unstable jet is therefore an ideal scenario in which to test Q_{GN} conservation. The evolution of a barotropically-unstable jet was presented as a useful test-case for numerical models of the shallow water equations on a sphere by Galewsky et al. [12]. Here, a similar test-case is proposed for the GN extended shallow water set. The existence of a conserved GN PV following the flow is central to the test.

A steady solution of the GN Eqs. (2a) and (2b) representing a barotropic jet in geostrophic balance may be specified analytically by

$$u(y) = \operatorname{sech}^2(y) - u_0, \tag{29a}$$

$$v(y) = 0, \tag{29b}$$

$$\sigma(y) = \frac{F^2}{\epsilon}(u_0 y - \tanh(y)) + 1, \tag{29c}$$

where the constant u_0 is given by

$$u_0 = \frac{\tanh(\pi)}{\pi},$$

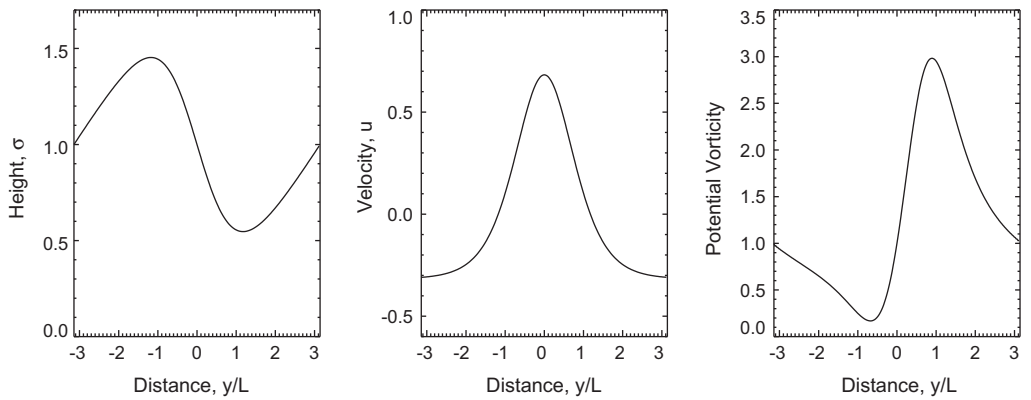

Fig. 3. The layer depth $\sigma(y)$ the velocity $u(y)$ and the GN potential vorticity $Q_{GN}(y)$ fields for the jet initial conditions defined by (29a)–(29c) with $F = 1.0$, $\epsilon = 1.0$.

to ensure that the mean u field is zero. The flow initially has zero divergence and the dispersive terms in (4a)–(4c) are zero. Eqs. (29a)–(29c) therefore satisfy the non-dispersive shallow water geostrophic balance condition

$$\sigma_y = -\frac{F^2}{\epsilon}u, \tag{30}$$

and the initial flow is therefore a steady solution of the GN Eqs. (4a)–(4c). The mean layer depth is unity and the parameter F^2/ϵ in (29c) controls the steepness of the height of the fluid layer in the initial conditions.

The initial jet is barotropically unstable. A small perturbation,

$$\sigma' = \sigma_p e^{-(x/\alpha_p)^2-(y/\beta_p)^2},$$

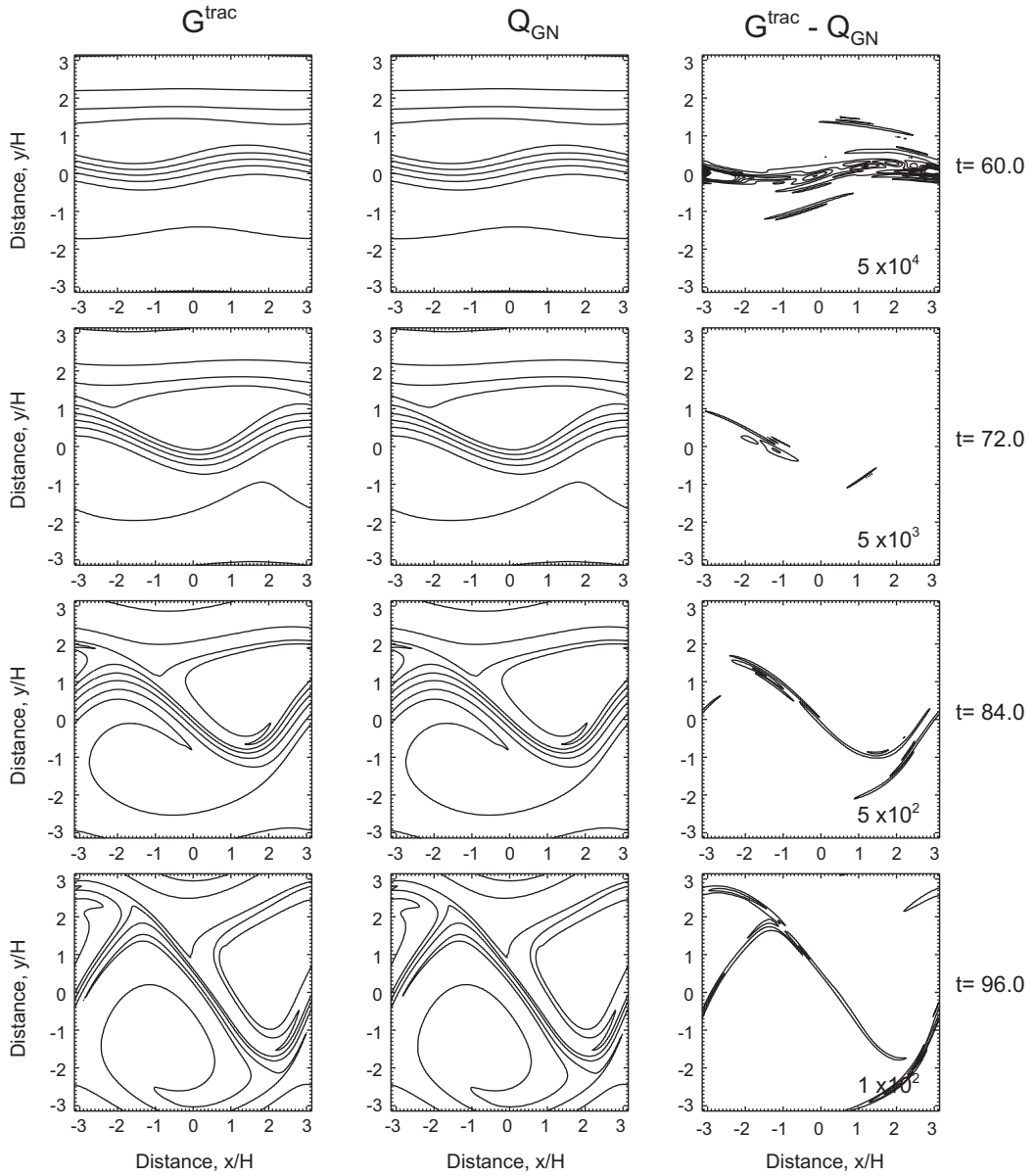

Fig. 4. Contour plots of the tracer $\mathcal{G}^{trac}$ (left column), the GN PV, Q_{GN}, (middle column) and the difference between these fields (right column) are shown at a resolution of 256 × 256 Fourier modes and for parameter values $F = 1$, $\nu = 1$ and $\epsilon = 1$. Dissipative terms have been added in accordance with Table 1 and $\gamma = 0.80$. Contours are shown at times t= 60, 72, 84 and 96 non-dimensional time units. The contour interval is 0.5 and in the right column the fields have been magnified by the factors shown.

where

$$\sigma_p = 0.01, \quad \alpha_p = \frac{\pi}{5}, \quad \beta_p = \frac{\pi}{5},$$

is added to the height field in (29c) to initiate the development of the barotropic instability. For the test-case explored here, the parameters F, ϵ and ν are set to unity in order that the free surface, rotational and dispersive terms are comparable.

A fixed value of the iteration damping coefficient γ is used for the integration. The optimum value of the iteration damping constant γ_{opt} found by repeating the numerical experiment, was $\gamma_{opt} \approx 0.80$. From (30), the maximum initial height gradient is $|\nabla\sigma|_{max} = u_0 \approx 0.32$, in excellent agreement with the left-hand panel of Fig. 2 and providing further evidence that this figure is a useful guide to setting the value of γ even for scenarios well-removed from the steadily propagating cnoidal waves of Section 4.3. To model the ensuing turbulent flow in two horizontal dimensions, it is necessary to add hyperdiffusion, as discussed in Section 3.3.

The parcel-wise conservation of the GN PV may be tested by obtaining Q_{GN} from the prognostic variables and comparing the time evolution of Q_{GN} to that of a tracer, $\mathcal{G}^{trac}$, whose value is obtained by numerically integrating the tracer advection equation

$$\mathcal{G}^{trac}_t = -\mathbf{u}\cdot\nabla\mathcal{G}^{trac} - \kappa\nabla^4\mathcal{G}^{trac}, \tag{31}$$

simultaneously with the GN equations in the numerical model. Eq. (31) is solved using a standard pseudo-spectral method following similar steps to those described for the GN equations in Section 3. The initial tracer field is set equal to the initial GN PV field, $\mathcal{G}^{trac}(\mathbf{x},0) = Q_{GN}(\mathbf{x},0)$, and as the hyperdiffusion acts only at scales near the grid-scale, it is expected that at larger scales the evolution of Q_{GN} will closely resemble that of $\mathcal{G}^{trac}$. The magnitude of the difference between these two fields is therefore a measure of the accuracy of the numerical code. A separate, but related issue, is to ensure that it is the full Green–Naghdi PV Q_{GN} that is conserved during the integration, as distinct from the SWE PV Q_{SW}. A second test is therefore to ensure that the relative magnitude of the pseudo-potential vorticity Q^* (given by (6)), which is zero initially, becomes appreciable during the integration, thus ensuring that the dispersive terms of the GN equations are simulated correctly.

To address the above issues it is useful to introduce the two diagnostics,

$$S_1(t) = \log_{10}\left(\frac{\int_D \sigma|Q_{GN} - Q_{SW}|d^2\mathbf{x}}{\int_D \sigma Q_{GN} d^2\mathbf{x}}\right),$$
$$S_2(t) = \log_{10}\left(\frac{\int_D \sigma|Q_{GN} - \mathcal{G}^{trac}|d^2\mathbf{x}}{\int_D \sigma Q_{GN} d^2\mathbf{x}}\right),$$

where $\int_D$ indicates integration over the entire domain. The diagnostic S_1 is a measure of the magnitude of the 'dispersive' part of the GN PV. The diagnostic S_2 is a measure of the relative magnitude of the difference between the GN PV and the tracer.

Fig. 3 shows the initial (basic state) profiles $\sigma(y)$, $u(y)$ and $Q_{GN}(y)$ of the barotropic jet. Initially $Q^* = 0$, so that $Q_{GN} = Q_{SW}$. Fig. 4 shows snapshots of the subsequent time evolution of the tracer $\mathcal{G}^{trac}$ (left column), the GN PV Q_{GN} (middle column) and the difference (right column, magnified by factor indicated). A model run at resolution of 256×256 Fourier modes is used, with κ as given in Table 1. Four different times are shown, spanning the early (near-linear) and later (nonlinear) stages of the development of the barotropic instability. The contours of $\mathcal{G}^{trac}$ and Q_{GN} are identical to the eye, even out to times when the development of the jet is clearly highly nonlinear. The difference field in the right column are dominated at all times by

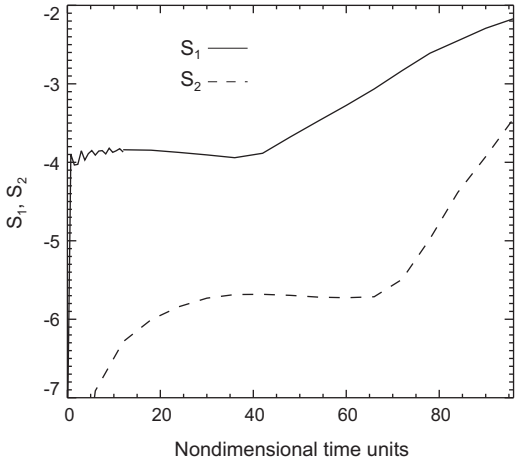

Fig. 5. The time evolution of the diagnostics S_1 (a measure of the relative importance of the pseudo-PV to Q_{GN}) and S_2 (a measure of the accumulated difference between the advected tracer and Q_{GN}, during the roll-up of the barotropically-unstable jet shown in Fig. 4 and defined initially by (29a)–(29c) with $F = 1$, $\nu = 1$ and $\epsilon = 1$.

features near the grid-scale concentrated on the jet core where hyperdiffusive tendencies are largest, confirming that Q_{GN} is accurately conserved by the algorithm except for the effects of the hyperdiffusion. This result is to be expected as hyperdiffusion acts indirectly on Q_{GN} through the σ, δ and ζ fields, but acts directly on $\mathcal{G}^{trac}$.

To demonstrate that the 'dispersive' part of the PV Q^* is significant and that it is indeed Q_{GN} rather than Q_{SW} which is conserved, the time evolution of the diagnostics S_1 and S_2 is shown in Fig. 5. The figure shows that S_1 is always around two orders of magnitude greater than S_2. Clearly, Q_{GN} is conserved more accurately, by two orders of magnitude, than Q_{SW}. Notably, Fig. 5 shows S_1 undergoing a rapid increase from zero at $t = 0$ to a value close to -4 immediately afterwards. The rapid increase in S_1 is due to the rapid 'geostrophic adjustment' of the small Gaussian perturbation in surface height that was added to initialise the instability. Inertia-gravity waves are radiated from the perturbation on the inertial timescale (1 time unit on Fig. 5). As the inertia-gravity waves propagate away, Q_{GN} is conserved following fluid parcels, but exchange takes place between its two components Q_{SW} and Q^*.

6. Conclusions

A new pseudo-spectral algorithm for the two-dimensional, rotating GN equations has been described. The numerical solutions presented include accurate simulations of both nonlinear solitary (strictly, cnoidal) waves and accurate parcel-wise conservation of the Miles–Salmon GN PV. The relative efficiency of the algorithm relative to a comparable pseudo-spectral algorithm for the shallow water equations is found to depend on typical values of the free surface slope. The free surface slope controls the convergence of an iteration in spectral space to find the divergence tendency, and for problems of interest that are within the range of validity of the GN approximation, the iteration is typically found to converge to an acceptable precision with 10 or fewer steps, independently of model resolution.

The GN equations are arguably the simplest hydrodynamic model having a realistic description of both nonlinear water waves and vortical dynamics. It is therefore intended that the new algorithm and the resulting numerical model will be of use to atmospheric scientists and oceanographers interested in exploring physical phenomena where both effects are important, for example, the generation of solitary waves at ocean ridges in a turbulent flow. More general questions, concerning the overall extent of the interaction between solitary waves and vortices, may also be answered.

Recent developments in the solution of the rotating shallow water equations [24,25] have focused on separating as far as possible the 'wave-like' (hyperbolic) and 'vortical' (elliptic) aspects of the problem. Following a transformation to a suitable set of prognostic variables, one of which is the PV, the system can be expressed as a pair of wave equations together with an advection equation for the PV. For a wide range of parameter settings, once the PV is associated with a 'balanced' velocity and height field, defined in terms of a suitable inversion operator acting on the PV field itself, the wave equations and PV advection equation are known to be only very weakly coupled. The advantages of such an approach are almost self-evident; separate and appropriate numerical methods can be used to tackle the wave equations and the PV advection/operator inversion components of the problem. The disadvantage of these methods is that the PV inversion operator is generally nonlinear and must be solved iteratively. A future extension of the present algorithm for the GN equations might involve solving the nonlinear iteration necessary to obtain the divergence tendency (or its analog under the variable transformation) in parallel with, and using similar algorithms to, the spectral PV inversion operation described in [24]. Such a development, whilst technically detailed, might allow the advantages of [24] approach to be adapted to the GN equations at little additional cost.

Appendix A. The numerical model of the Green–Naghdi equations with topography

In the presence of bottom topography the rotating GN equations are given in vector form by

$$D\mathbf{u} + f\mathbf{k}\times\mathbf{u} + g\nabla(\sigma + b) = -\frac{1}{\sigma}\nabla\left(\sigma^2\left[\frac{D^2 b}{2} - \frac{D(\sigma\delta)}{3}\right]\right) - \nabla b\left[D^2 b - \frac{D(\sigma\delta)}{2}\right],$$

$$D\sigma + \sigma\delta = 0,$$

where the function $b(\mathbf{x})$ defines the bottom topography. Using the non-dimensionalization defined by (1) and also scaling the topography with the height so that $b = Hb^*$, we obtain (dropping asterisks)

$$D\mathbf{u} + \frac{\mathbf{k}\times\mathbf{u}}{\epsilon} + \frac{\nabla(\sigma + b)}{F^2} = -\frac{v}{\sigma}\nabla\left(\sigma^2\left[\frac{D^2 b}{2} - \frac{D(\sigma\delta)}{3}\right]\right) - v\nabla b\left[D^2 b - \frac{D(\sigma\delta)}{2}\right], \tag{A.1}$$

$$D\sigma + \sigma\delta = 0.$$

Applying the operators $\nabla\cdot$ and $\mathbf{k}\cdot\nabla\times$ to (A.1) and using the fact that

$$\frac{1}{\sigma}\nabla\left(\sigma^2\left[\frac{D^2 b}{2} - \frac{D(\sigma\delta)}{3}\right]\right) = \nabla\left(\sigma\left[\frac{D^2 b}{2} - \frac{D(\sigma\delta)}{3}\right]\right) + \nabla\sigma\left[\frac{D^2 b}{2} - \frac{D(\sigma\delta)}{3}\right],$$

the equations may be recast in vorticity–divergence form

$$\delta_t = \mathbf{k}\cdot\nabla\times(\mathbf{u}(\zeta+\epsilon^{-1})) - \nabla^2\left(\frac{\sigma+b}{F^2}+\frac{\mathbf{u}\cdot\mathbf{u}}{2}+\nu\sigma\left[\frac{D^2b}{2}-\frac{D(\sigma\delta)}{3}\right]\right)$$
$$-\nabla\cdot\left(\nu\nabla\sigma\left[\frac{D^2b}{2}-\frac{D(\sigma\delta)}{3}\right]+\nu\nabla b\left[D^2b-\frac{D(\sigma\delta)}{2}\right]\right),$$
$$\zeta_t = -\nabla\cdot(\mathbf{u}(\zeta+\epsilon^{-1})) - \mathbf{k}\cdot\nabla\times\left(\nu\nabla\sigma\left[\frac{D^2b}{2}-\frac{D(\sigma\delta)}{3}\right]+\nu\nabla b\left[D^2b-\frac{D(\sigma\delta)}{2}\right]\right),$$
$$\sigma_t = -\nabla\cdot(\sigma\mathbf{u}).$$

The second order advective derivative D^2b may be written in vector form as

$$D^2b = \mathbf{u}_t\cdot\nabla b + \mathbf{u}\cdot[(\mathbf{u}\cdot\nabla)\nabla b + (\nabla b\cdot\nabla)\mathbf{u} + \nabla b\times(\nabla\times\mathbf{u})],$$

introducing $\mathbf{u}_t$ into the equations. In Section 3, it was demonstrated that the GN equations could be solved in the absence of topography by using the divergence equation to iterate towards the correct value of δ_t at each time-step. The appearance of $\mathbf{u}_t$ in the equations in the presence of topography means that there are now two unknown quantities in the divergence equation. We nevertheless proceed with an iteration to find δ_t in the same manner as in the case of zero topography in Section 3 and use the values of $\mathbf{u}_t$ from the previous time-step. This approach is justified by the fact that a small error on one of the relatively small dispersive terms is negligible in its effect on the value of δ_t obtained by the iteration. Following a similar course to Section 3, we split the terms in the GN equations into those involving δ_t and those not by defining

$$\mathbf{E} = \mathbf{u}(\zeta+\epsilon^{-1}),$$
$$\mathbf{G} = -\nu\nabla\sigma\left[\frac{D^2b}{2}+\frac{\sigma\delta^2-\sigma(\mathbf{u}\cdot\nabla)\delta}{3}\right]-\nu\nabla b\left[D^2b+\frac{\sigma\delta^2-\sigma(\mathbf{u}\cdot\nabla)\delta}{2}\right],$$
$$\mathbf{H} = \nu\sigma\delta_t\left(\frac{\nabla b}{2}+\frac{\nabla\sigma}{3}\right),$$
$$\mathbf{L} = \sigma\mathbf{u},$$
$$\mathcal{T} = -\frac{\mathbf{u}\cdot\mathbf{u}}{2}-\frac{\sigma+b}{F^2}-\nu\sigma\left[\frac{D^2b}{2}+\frac{\sigma\delta^2-\sigma(\mathbf{u}\cdot\nabla)\delta}{3}\right],$$
$$\mathcal{W} = \frac{\nu\delta_t}{3}(\sigma^2-1),$$

so that, (9)–(11) are satisfied by $\mathcal{T}$ and $\mathcal{W}$, as defined above, and $\mathcal{N}, \mathcal{Q}, \mathcal{P}, \mathcal{M}, \mathcal{R}$ and $\mathcal{S}$, as defined by (8), using the new expressions for **E**, **G**, **H** and **L** above. From (11) onwards explanation of the numerical scheme with topography then proceeds in exactly the same way as for the zero topography case in Section 3 with the new expressions for **E**, **G**, **H**, **L**, $\mathcal{T}$ and $\mathcal{W}$ above being assumed.

References

[1] R. Asselin, Frequency filter for time integrations, Mon. Weather Rev. 100 (1972) 487–490.
[2] S.V. Bazdenkov, N.N. Morozov, O.P. Pogutse, Dispersion effects in the two-dimensional hydrodynamics, Sov. Phys. Dokl. 32 (1987) 262.
[3] J.P. Boyd, Chebyshev and Fourier Spectral Methods, second ed., Dover Publications, New York, 2001.
[4] W. Choi, R. Camassa, Fully nonlinear internal waves in a two-fluid system, J. Fluid Mech. 396 (1999) 1–36.
[5] P.J. Dellar, Dispersive shallow water magnetohydrodynamics, Phys. Plasmas 10 (2003) 581–590.
[6] P.J. Dellar, R. Salmon, Shallow water equations with a complete coriolis force and topography, Phys. Fluids 17 (2005) 106601–106619.
[7] G.A. El, R.H.J. Grimshaw, N.F. Smyth, Unsteady undular bores in fully nonlinear shallow-water theory, Phys. Fluids 18 (2006).
[8] G.A. El, R.H.J. Grimshaw, N.F. Smyth, Transcritical shallow-water flow past topography: finite-amplitude theory, J. Fluid Mech. 640 (2009) 187–214.
[9] R.C. Ertekin, Soliton generation by moving disturbances in shallow water: theory, computation and experiment. Ph.D. Dissertation, University of California, Berkeley, 1984.
[10] R.C. Ertekin, W.C. Webster, J.V. Wehausen, Ship-generated solitons, in: Proc. 15th Symp. Naval Hydrodynamics, National Academy of Sciences, Washington, DC, 1984.
[11] R.C. Ertekin, W.C. Webster, J.V. Wehausen, Waves caused by a moving disturbance in a shallow channel of finite width, J. Fluid Mech. 169 (1986) 275–292.
[12] J. Galewsky, R.K. Scott, L.M. Polvani, An initial-value problem for testing numerical models of the global shallow-water equations, Tellus 56 (2004) 429–440.
[13] S.L. Gavrilyuk, V.M. Teshukov, Generalized vorticity for bubbly liquid and dispersive shallow water equations, Continuum Mech. Thermodyn. 13 (2001) 365.
[14] A.E. Green, P.M. Naghdi, A derivation of equations for wave propagation in water of variable depth, J. Fluid Mech. 78 (1976) 237–246.
[15] J.J. Hack, R. Jakob, Description of a global shallow water model based on the spectral transform method, NCAR Technical Note NCAR/TN-343+STR (unpublished), 1992.
[16] K.R. Helfrich, Decay and return of internal solitary waves with rotation, Phys. Fluids 19 (2003) 026601.
[17] K.R. Helfrich, R.H. Grimshaw, Nonlinear disintegration of the internal tide, J. Phys. Ocean. 38 (2008) 686–701.
[18] K.R. Helfrich, W.K. Melville, Long nonlinear internal waves, Annu. Rev. Fluid Mech. 38 (2006) 395–425.
[19] B.J. Hoskins, M.E. McIntyre, W.A. Robertson, On the use and significance of isentropic potential–vorticity maps, Q. J. R. Met. Soc. 111 (1985) 877–946.

[20] R. Jakob, J.J. Hack, D.L. Williamson, Solutions to the shallow water test set using the spectral transform method, NCAR Technical Note NCAR/TN-388+STR, NTIS PB93-202729 (unpublished), 1993.
[21] Y.A. Li, Hamiltonian structure and linear stability of solitary waves of the Green–Naghdi equations, 2002.
[22] O. Le Métayer, S. Gavrilyuk, S. Hank, A numerical scheme for the Green–Naghdi model, J. Comp. Phys. 229 (2010) 2034–2045.
[23] J. Miles, R. Salmon, Weakly dispersive nonlinear gravity waves, J. Fluid Mech. 157 (1985) 519–531.
[24] A.R. Mohebalhojeh, D.G. Dritschel, On the representation of gravity waves in numerical models of the shallow water equations, Q. J. R. Met. Soc. 126 (2000) 669–688.
[25] A.R. Mohebalhojeh, D.G. Dritschel, Assessing the numerical accuracy of complex spherical shallow water flows, Mon. Weather Rev. 135 (2007) 3876–3894.
[26] B.T. Nadiga, L.G. Margolin, P.K. Smolarkiewicz, Different approximations of shallow fluid flow over an obstacle, Phys. Fluids 8 (1996) 2066–2077.
[27] A. Robert, The integration of a spectral model of the atmosphere by the implicit method, in: Proc. WMO/IUGG Symposium on NWP, Tokyo, Japan Meteorological Agency, vol. VII, 1969, pp. 19–24.
[28] C.H. Su, C.S. Gardner, Korteweg–de Vries equation and generalizations. iii. Derivation of the Korteweg–de Vries equation and burgers equation, J. Math. Phys. 10 (1969) 536.
[29] G.K. Vallis, Atmospheric and Oceanic Fluid Dynamics, Cambridge University Press, Cambridge, UK, 2006.
[30] G.B. Whitham, Linear and Nonlinear Waves, John Wiley and Sons, London, 1974.